

Covalent organic frameworks with high quantum efficiency in photocatalytic hydrogen evolution: mediating charge separation

Chunzhi Li

Dalian Institute of Chemical Physics

Jiali Liu

Dalian Institute of Chemical Physics

He Li (✉ liwe@dicp.ac.cn)

Dalian Institute of Chemical Physics <https://orcid.org/0000-0003-0830-0844>

Kaifeng Wu

Dalian Institute of Chemical Physics, Chinese Academy of Sciences <https://orcid.org/0000-0002-1047-6606>

Junhui Wang

Dalian Institute of Chemical Physics, Chinese Academy of Sciences <https://orcid.org/0000-0002-9314-143X>

Qihua Yang

Dalian Institute of Chemical Physics <https://orcid.org/0000-0002-1118-3397>

Article

Keywords: charge carrier lifetime, β -ketene-CN, CN-CON

Posted Date: November 1st, 2021

DOI: <https://doi.org/10.21203/rs.3.rs-1020038/v1>

License:   This work is licensed under a Creative Commons Attribution 4.0 International License.

[Read Full License](#)

Abstract

Compared with inorganic semiconductors, the difficulty of exciton dissociation is one of the main reasons for the lower photocatalytic activity of organic semiconductors. In this work, we report that the charge carrier lifetime is dramatically prolonged by incorporating a suitable donor-acceptor (β -ketene-CN) pair to a covalent organic framework nanosheet (CN-CON). CN-CON showed remarkably high apparent quantum efficiency up to 82.6% at 450 nm in photocatalytic H_2 evolution, superior to all the COFs reported so far. The charge carrier kinetic analysis and femtosecond transient absorption spectroscopy characterizations verified that CN-CON had intrinsically lower exciton binding energies and hence longer-lived charge carriers than the corresponding CON without CN unit. This work provides an excellent model for gaining insight into the nature of ultrashort-lived active species in polymeric organic photocatalysts.

Introduction

Photocatalytic water splitting to produce H_2 is a sustainable way to convert solar energy into clean chemical energy, which helps to solve the current energy crisis and environmental issues. Since 1970s, scientists all over the world have been making endless attempts to obtain this “holy grail” which is destined to shine through the annals of scientific history.^[1-7] Very promisingly, Takata and co-authors reported that the apparent quantum efficiency (AQE) of almost unity was achieved over $SrTiO_3$ for overall water splitting irradiated with the light in the ultraviolet region by selecting suitable cocatalyst and fully promoting the spatial separation of charge carriers among different crystal facets.^[8] Due to the fact that the visible light occupies 42-45% in the solar spectrum,^[9-11] the development of visible-light responsive photocatalysts is necessary for the efficient use of solar energy. Up to date, the inorganic semiconductors (ISs) dominate in the photocatalytic water splitting, but the visible light responsive ISs with suitable band structure for water splitting is still very limited which is related with the difficulties in the band structure engineering.

Covalent organic frameworks (COFs) as a kind of organic polymers have gradually shined in the fields of gas separation,^[12-14] energy storage,^[15-18] sensors,^[19-22] and catalysis.^[23-30] Especially, the two-dimensional (2D) COFs with extended π - π conjugation structure have great application potential in photocatalysis. One of the unique advantages is that the band structure of 2D COFs can be finely tuned at molecular level by means of incorporation of different organic building blocks. Though 2D COFs favor some essential photocatalysis steps, such as, light trapping, charge separation and charge carrier migration, most of 2D COFs exhibit only moderate photocatalytic activities, especially in comparison with ISs, which is possibly related with the high exciton binding energy and fast charge recombination.^[31] It was reported that the excitons dissociation ability of 2D COFs could be improved by incorporating donor-acceptor (D-A) structure, enhancing the network polarity and reinforcing the conjugation structure.^[32-34] Thus, triazin-containing,^[35] halogen-containing,^[36] sulfone-containing,^[37] and sp^2 carbon-conjugated^[38, 39] COFs have been synthesized and they show enhanced hydrogen evolution reaction (HER) activities. Nevertheless, the AQE of 2D COFs is not high in HER and there is still a big room for improvement. There

are few studies on the exciton and charge carrier kinetics of COFs, which are critical for understanding the essential steps in photocatalysis and for the design of COFs as efficient photocatalysts.^[40] The current research progresses in the organic photocatalysts, such as dye molecule, conjugated polymers, g-C₃N₄, are far left behind with respect to photocatalytic activity as well as mechanism study compared to ISs.^[41]

Cyano moiety, as an electron-withdrawing group, has been widely introduced in classical non-fullerene acceptors, such as ITIC and Y6.^[42, 43] Optimized photovoltaic devices, such as ITO/PEDOT:PSS/PM6:Y6/PDINO/Al, exhibit efficient device performance with power conversion efficiencies (PCEs) up to 15.7%,^[44] largely because of choosing suitable D-A structure to promote the separation of charges which is also a critical step in photocatalysis. Cyano moiety appears in recent reported COFs for photocatalytic HER, such as, sp² carbon-conjugated COFs based on Knoevenagel condensation reaction and CTFs based on benzonitrile trimerization reaction.^[40, 45] Still, these COFs do not possess high AQE or photocatalytic HER activity, which is possibly related with the inefficient D-A pair.

In this work, we synthesized a β -ketoenamine linked CN-COF with ketene-CN (D-A) pair via a Schiff-base condensation reaction of 1,3,5-triformylphloroglucinol (Tp) with 4,4'-diamino-[1,1'-biphenyl]-3,3'-dicarbonitrile (BDCN). CN-COF (COFs nanosheet obtained by ball milling of CN-COF) afforded extremely high AQE up to 82.6% at 450 nm, a record-breaking AQE for hydrogen evolution for the COF-based photocatalysts as far as we know. The whole picture of exciton dissociation and charge recombination was elucidated with temperature-dependent photoluminescence and femtosecond transient absorption (fs-TA) measurements.

Results

Designed synthesis and characterizations. CN-COF was synthesized via a Schiff-base condensation reaction of 1,3,5-triformylphloroglucinol (Tp) with 4,4'-diamino-[1,1'-biphenyl]-3,3'-dicarbonitrile (BDCN) in the presence of 6 M aqueous acetic acid (Fig. 1a). The formation of β -ketoenamine linkage via a keto-enol tautomerization could increase the chemical stability of CN-COF and the ketene can also serve as an electron donor. Thus, a ketene-CN D-A pair was successfully incorporated in CN-COF, which was further confirmed by the computational study of charge distribution (Fig. 1b). A control sample, BD-COF with similar linkage and topology structure to CN-COF but without cyano as acceptor, was synthesized according to literature method using Tp and benzidine (BD) as monomers.^[46]

The FT-IR spectrum of CN-COF displayed vibration peaks at 1618 cm⁻¹ and 1579 cm⁻¹ respectively assigned to the C=O and C=C stretching vibrations together with aromatic ring skeleton vibrations at 1494 cm⁻¹ and 1443 cm⁻¹, showing the formation of β -ketoenamine linkage (Fig. 1c).^[46, 47] Notably, the typical C \equiv N stretching vibration appeared at 2200 cm⁻¹, indicating that cyano groups can endure the synthesis condition without decomposition. Further, ¹³C CP-TOSS NMR spectrum of CN-COF provided strong supportive structure information with apparent chemical shift for -C=O at 184 ppm, -NH-C=C at 149 ppm and 104 ppm, C \equiv N at 114 ppm and aromatic rings in the range of 150 to 95 ppm (Fig. 1d). All

data above provided adequate chemical composition evidence for the successful preparation of CN-COF with cyano groups. The FT-IR spectrum of BD-COF was in accordance with a previous report,^[46] showing the presence of vibrations associated with β -ketoenamine structure (Supplementary Fig. 1). CN-COF and BD-COF with decomposition temperature beyond 350 °C in flowing air had high thermal stability evaluated by thermogravimetric analysis (TGA) (Supplementary Fig. 2).

The crystalline nature of CN-COF was characterized by powder X-ray diffraction (PXRD) technique. The PXRD pattern of CN-COF exhibited a predominant peak at 3.60°, corresponding to the reflection of (100) plane, with other weak peaks at 6.25°, 7.18° and a broad peak at 26.5°, which can be assigned to the (110), (200) and (001) plane, respectively (Fig. 1e). Furthermore, Pawley refinement confirmed that the diffraction patterns of CN-COF were consistent with a hexagonal lattice with P6/M space group ($a = b = 28.78 \text{ \AA}$, $c = 3.60 \text{ \AA}$; $\alpha = \beta = 90^\circ$, $\gamma = 120^\circ$; $R_p = 3.99\%$, $R_{wp} = 4.91\%$) similar to an eclipsed model (Supplementary Table 1, Fig. 1e). A poor correlation with crystallographic structures of CN-COF was obtained with staggered AB model (Supplementary Table 2, Supplementary Fig. 3), further confirming the eclipsed AA stacking model of CN-COF. Analogously, the PXRD patterns of BD-COF were consistent with previous report,^[46] showing the eclipsed AA stacking model (Supplementary Fig. 4). In comparison with CN-COF, the (001) diffraction of BD-COF shifted to higher 2-theta angle, indicating that the interlayer distance of BD-COF was smaller than that of CN-COF, likely due to the increased charge repulsion between interlayer with the existence of strong polar cyano group.^[48] All organic semiconductors displayed quite different diffraction peaks with monomers, demonstrating the successful formation of corresponding polymer without residual monomers (Supplementary Fig. 4).

The Brunauer–Emmett–Teller (BET) surface area of CN-COF measured by nitrogen sorption isotherms at 77 K was 559 m² g⁻¹ with the pore size ranging from 1.0 to 2.5 nm calculated by nonlocal density functional theory (NLDFE) method (Supplementary Table 3, Supplementary Fig. 5). The BD-COF has a BET surface area of 519 m² g⁻¹ with pore size distribution from 1.0 to 2.5 nm (Supplementary Table 3, Supplementary Fig. 5). The scanning electron microscopy (SEM) images of both CN-COF and BD-COF depicted the rod-like morphology (Supplementary Fig. 6). After ball milling, CN-CON and BD-CON were obtained. The TEM images of CN-CON and BD-CON showed almost identical nanosheet morphology with lateral sizes close to 500 nm (Supplementary Fig. 7). The periodic framework structure of CN-CON was visualized by high-resolution transmission electron microscopy (HRTEM). The hexagonal straight pore feature of CN-CON can be clearly observed (Fig. 2a). Fourier-filtered image of enlarged red square area showed that the interplanar spacing of (100) lattice plane was calculated to be 2.3 nm, consistent with the pore size by N₂ sorption isotherm and simulated eclipsed model (Fig. 2b). The atomic force microscopy (AFM) images of both CONs drop-coated onto mica from ethanol suspensions also displayed nanosheet morphology with thickness ranging from 2 to 3 nm, corresponding to the existence of only ~6-9 COF layers (Fig. 2c). The PXRD patterns and pore size distributions of CN-CON and BD-CON after ball milling were identical to pristine COFs, indicating that COFs can endure the high-energy ball milling process because of the high thermostability (Supplementary Fig. 4). The BET surface area of CONs decreased as compared with the pristine COFs due to the exfoliated ultra-thin nanosheet effect.^[49] Both

CONs can be well dispersed in water to form colloid solution as verified by the conspicuous Tyndall effect, and colloid solution remains stable even over 4 months (Fig. 2e, Supplementary Fig. 8). The dynamic light scattering (DLS) measurement showed the dominant colloid size distribution at ~ 530 nm for both CONs coincided with corresponding TEM results (Fig. 2e, Supplementary Fig. 7 and 8). All evidences above proved that the 2D CONs were successfully obtained by mechanical exfoliation of bulk COFs.

The chemical stability of CN-COF under harsh condition, especially under prolonged light irradiation, is the prerequisite for photocatalysis application. To our delight, CN-COF could withstand different harsh conditions, such as upon 3-day immersion in THF, DMSO, DMF, 3 M aqueous HCl, and 3 M NaOH, as evidenced by the almost identical PXRD patterns and FT-IR spectra before and after treatments (Supplementary Fig. 9). Even after 3-day Xenon lamp irradiation in water, no obvious changes in PXRD pattern or FT-IR spectrum could be observed for CN-COF (Supplementary Fig. 9). The above results revealed the excellent chemical stability and photo-stability of CN-COF.

Photocatalytic hydrogen evolution reaction. The UV-vis diffusion reflectance spectroscopy (DRS) spectrum of CN-COF exhibited an absorption band with edges at 627 nm, implying the obvious visible light responsive nature (Fig. 3a). In comparison with BD-COF, CN-COF presented apparent red shifts. It is well established that the absorption edge of π conjugated systems will red shift with the incorporation of chromophore in frameworks.^[50] The optical band gaps of CN-COF and BD-COF were calculated to be 2.17 and 2.24 eV by Tauc plots, respectively (Supplementary Fig. 10). This result indicated that cyano groups could narrow the band gap, as a result, increasing light trapping ability. Furthermore, the conduction band (CB) and valence band (VB) positions of the two COFs estimated by electrochemical Mott-Schottky plots and their optical band gaps were enough for both proton reduction and water oxidation reaction (Supplementary Fig. 10). The positive slope of Mott-Schottky plots indicated typical n-type semiconductor feature for both COFs. CN-COF exhibited more negative CB position than that of BD-COF, implying stronger driving force for proton reduction.

We next evaluated the activity of CN-COF for HER under visible light ($\lambda > 420$ nm). The loading amount of Pt and different types of sacrificial reagent (sodium ascorbate, Na_2SO_3 or TEOA) were screened first (Supplementary Table 4, Supplementary Fig. 11). 1 wt% Pt with 0.1 M ascorbic acid as a sacrificial reagent was the optimized reaction conditions for CN-COF. Notably, no obvious change in Pt size was observed with the Pt loading used for the test (Supplementary Fig. 11). The volcano curve of HER rate and Pt loading implied the combined effect of the electron trapping for proton reduction and light absorbance by Pt. Under optimized conditions, the average H_2 evolution rate of CN-COF and BD-COF was 1217 and 39.5 $\mu\text{mol h}^{-1}$ (Fig. 3b), respectively. Thirty-folds increasing of H_2 evolution rate of CN-COF in comparison with BD-COF demonstrated the promotion effect of cyano groups in photocatalytic HER.

Amazingly, the photocatalytic HER rate of CN-COF was as high as 2684 $\mu\text{mol h}^{-1}$ (normalized by mass: 134200 $\mu\text{mol g}^{-1} \text{h}^{-1}$), more than twice that of CN-COF. The BD-COF also showed an increased hydrogen production rate (159 $\mu\text{mol h}^{-1}$), which was 4 times higher than that of pristine bulk COF. The enhanced

hydrogen production rate of the several-layered nanosheet as compared with the bulk COFs was related with the short migration distance of photogenerated charge carriers and also more exposing reaction surface.^[51,52] Deuterium isotope experiments were carried out using D₂O, and the evaluated gases were detected by mass spectrometry (MS). Nearly all mass-to-charge contributions are D₂, indicating that the produced H₂ was indeed from water molecules (Supplementary Fig. 12). The AQE as high as 82.6% at 450 nm (Fig. 3c) was achieved for CN-CON. The AQE decreased as the wavelength of the irradiation light increasing, identical to the light adsorption properties of CN-CON. Notably, the AQE as high as 4.2% could still be obtained even irradiated with 650 nm red light, implying the efficiency of CN-CON in photocatalytic HER. In the literature, the photocatalytic activity was always compared using H₂ evolution rate normalized by the mass of the photocatalyst. In fact, this is not a right way due to the fact that the H₂ evolution amounts do not increase linearly with the content of photocatalyst and AQE is a suitable parameter for comparing the photocatalytic activity, as pointed out by Prof. C. Li and Prof. K. Domen recently.^[53] We summarized the reported AQE and photocatalytic activity of COFs and polymers in H₂ evolution reaction (Fig. 3d, Supplementary Table 5 and 6).^[32-39,54-66] As compared with the reported COF/polymer-based photocatalyst, CN-CON showed the highest AQE as far as we know, which was in a comparable level to that of previously reported star inorganic Pt-PdS/CdS photocatalyst.^[4] Even comparing with the H₂ evolution rate normalized by the mass, CN-CON is superior to most of the COFs/polymer-based photocatalyst.

The long-term cycling experiment with CN-CON as model catalyst showed no obvious decline in H₂ production rate for more than 24 h (Fig. 3e) and the PXRD pattern and FT-IR spectrum of CN-CON remained almost the same before and after photocatalysis (Supplementary Fig. 13), signifying the excellent stability of CN-CON for photocatalysis. We also drop-casted Pt-CN-CON colloid solution onto a glass support (size of 1 cm × 6 cm, Supplementary Fig. 14). Hydrogen bubbles could be clearly observed over CN-CON film under visible light irradiation for 10 h (Supplementary Fig. 14, Supplementary Video). The average HER rate of CN-CON film can reach to 292 mmol m⁻², much higher than the reported COF film.^[37]

Incidentally, the photocatalytic oxygen evolution reaction (OER) was also performed here. To our delight, CN-CON could catalyze photocatalytic OER to afford OER rate of 1.933 μmol h⁻¹ with Co_xO_y as co-catalyst and AgNO₃ as electron sacrificial reagent (Supplementary Fig. 15). The ¹⁸O-labeled water experiment confirmed that the oxygen was sourced from water. The reason of relatively low OER rate may be due to the less positive valence band position of CN-CON (1.28 eV vs water oxidizing potentials 1.23 eV, pH = 0) and the sluggish four-electron transfer kinetic process of oxygen generation.

Mechanistic studies to uncover the role of CN. CN-CON afforded much higher activity than BD-CON though the two CONs have similar BET surface area, pore size and topology structure. The above electrochemical and optical characterization results revealed that the existence of CN would lead to an increase of light trapping and a negative shift of CB position. However, these thermodynamic properties

did not allow for any insight into the exciton and charge carriers properties, which are important for understanding the photocatalysis process.

To understand the exciton properties of CONs, temperature-dependent photoluminescence (PL) measurement was carried out to measure the exciton binding energies. The integrated PL intensity of both CONs decreased with increasing temperature from 77 K to 253 K, which can be mainly attributed to the thermally activated nonradiative recombination process (Fig. 4a, 4c).^[32,41,67] Further, based on a simple model, the temperature dependent PL intensity of two CONs can be expressed by the following equation:

$$I(T) = \frac{I_0}{1 + Ae^{-E_b/k_B T}}$$

where I_0 is the intensity at 0 K, E_b is the binding energy, A is a proportional constant and k_B is the Boltzmann constant.^[67,68] By fitting the experimental data, the exciton binding energies of CN-CON and BD-CON were estimated to be 31.2 and 44.2 meV, respectively (Fig. 4b, 4d), demonstrating that the excitons of CN-CON were more prone to dissociation than that of BD-CON, and thus improved the ratios of free charge carriers for CN-CON and contributed to its high photocatalytic activity.

Further, femtosecond transient absorption (fs-TA) measurements were applied to investigate in photocatalysis difference between the two COFs. First, a typical colloidal CN-CON sample was excited using a 400 nm pump pulse, and the TA spectra was acquired with a broadband probe pulse (Fig. 5a). The spectra exhibited a broad negative bleaching signal in the range of 420-540 nm assigned to the ground state bleach (GSB), which indeed coincided with the steady-state absorption spectra (Supplementary Fig. 16). In addition, the spectra were also characterized by a weak and broad positive signal (from 550 to 750 nm) (Fig. 5a). This positive signal could be attribute to trapped carriers (so-called "polarons" in polymers), because its formation was complementary to the decay of the GSB signal within 0.8 ps (Fig. 5b). The trapped carriers could be further assigned specifically as trapped holes on the basis of their rapid decay in the presence of the hole scavenger AA. As shown in Supplementary Fig. 17, these trapped holes were transferred to AA in < 2 ps. Following the initial hole trapping process, the holes and electrons recombined slowly, leading to the simultaneous decay of the hole signal and a negative broad feature centered at ~560 nm. The latter was likely assignable to the stimulated emission of the trapped exciton, as its spectral feature coincided with the steady-state PL spectra (Supplementary Fig. 18).

The lifetime of charge carriers was studied by TA kinetics of CONs. As shown in Fig. 5c, the decay curves for trapped hole of two CONs revealed significantly different lifetimes. The lifetime of CN-CON (14.2 ± 2.3 ps) was three times longer than that of BD-CON (4.3 ± 0.6 ps). The longer charge carrier lifetime will decrease the probability of electron-hole recombination which is a competitive and detrimental process in real photocatalysis system. Notably, after quenching the holes with AA, a new broad negative signal ranged from 500 to 750 nm clearly emerged within ns time scale, attributed to the generation of long-lived

free electrons (Supplementary Fig. 19). Fitting kinetics revealed that long-lived electrons of CN-COF had a much slower rate constant ($k_e = 1.3 \text{ ns}^{-1}$) than that of BD-COF ($k_e = 5.3 \text{ ns}^{-1}$) (Fig. 5d), which correlated well with H_2 production activity. All the observations indicated that the existence of CN can effectively extend the life-time of charge carriers and eventually increase the photocatalytic hydrogen evolution activity.

Discussion

In summary, we synthesized a novel CN-COF with β -ketene-CN as D-A pair for photocatalytic HER. Thirty-folds increase of H_2 evolution rate of CN-COF in comparison with BD-COF demonstrated the promotion effect of cyano groups in photocatalytic HER. More than two-fold increase in photocatalytic HER rate was observed by decreasing the COF layer number to ~ 6 -9 layers. An extremely high AQE up to 82.6% at 450 nm was obtained for CN-COF, superior to all currently reported polymer semiconductors to our knowledge. CN-COF possessed intrinsically lower exciton binding energy in comparison with BD-COF as demonstrated by temperature-dependent PL spectra. Moreover, the fs-TA spectroscopy characterizations revealed that the existence of CN can dramatically extend the life-time of charge carriers. The high charge separation efficiency may be the main reason for the excellent photocatalytic HER activity of CN-COF. Our results showcased the importance of the suitable D-A pair in charge separation and migration, a critical step in photocatalysis and shed light on the polymer semiconductors as promising photocatalysts.

Methods

Synthesis of BD-COF and CN-COF. A 10 mL high-pressure flask was charged with 1,3,5-triformylphloroglucinol (168 mg, 0.8 mmol) and diamine (1.2 mmol). A mixture of 1,4-dioxane and mesitylene (1:1 v/v, 8.0 mL) was added, and the resulting suspension was sonicated at room temperature for 10 min. 6 M aqueous acetic acid (2 mL) were added, and the resulting suspension was further sonicated for 10 min. The flask was degassed through three freeze-pump-thaw cycles to remove the dissolved oxygen. After warm to room temperature, the flask was charged with N_2 and sealed under positive N_2 pressure, and then placed (no stirring) in a 120 °C pre-heated oil bath for three days. After that, the obtained solid was washed with DMF, acetone and THF for several times and extracted by Soxhlet extraction using THF for 1 day, followed by drying under vacuum at 120 °C overnight to get corresponding COFs in $\sim 80\%$ isolated yield.

Synthesis of covalent organic nanosheets (CONs) from COFs by ball milling method. 150 mg of as-synthesized COFs were placed into a ball mill jar equipped with suitable amount zirconia balls (24 balls for $\Phi = 3 \text{ mm}$ and 6 balls for $\Phi = 6 \text{ mm}$) and then the mixture was milled at 50 Hz (planetary ball mill) for 30 min. The obtained CONs were collected without additional treatment. For TEM and AFM imaging, 1 mg of CONs was dispersed in 10 mL of ethanol and sonicated for 30 minutes and subsequently coated

on the carbon-coated copper grid (TEM) and mica (AFM). The solution was allowed to naturally volatilize overnight at room temperature prior to next measurement.

Photocatalytic hydrogen evolution. A flask with quartz filter was charged with the COFs (20 mg), 0.1 M ascorbic acid water solution (100 mL), and appropriate amount of H_2PtCl_6 as a co-catalyst. The resulting mixture was sonicated for 10 minutes before degassing by Ar bubbling for 30 minutes. The reaction system was irradiated with a 300 W Xe lamp (PLS-FX300, Perfectlight) for the time specified using cut-on filters ($\lambda > 420$ nm). Gas samples were taken with a gas-tight syringe (Hamilton 1700) and run on a gas chromatograph (Agilent 8860) equipped with Molecular Sieve 5A column connected to thermal conductivity detector. After the photocatalysis experiment, the photocatalyst were recovered by washing with water and ethanol then dried under vacuum at room temperature for 5 h for the next round of photocatalysis.

Data availability

All data that support the findings of this study are available from the corresponding author upon reasonable request.

References

1. Fujishima, A. & Honda, K. Electrochemical photolysis of water at a semiconductor electrode. *Nature* **238**, 37–38 (1972).
2. Yi, Z. et al. An orthophosphate semiconductor with photooxidation properties under visible-light irradiation. *Nat. Mater.* **9**, 559–564 (2010).
3. Wang, X. et al. A metal-free polymeric photocatalyst for hydrogen production from water under visible light. *Nat. Mater.* **8**, 76–80 (2009).
4. Yan, H. et al. Visible-light-driven hydrogen production with extremely high quantum efficiency on Pt–PdS/CdS photocatalyst. *J. Catal.* **266**, 165–168 (2009).
5. Hisatomi, T., Kubota, J. & Domen, K. Recent advances in semiconductors for photocatalytic and photoelectrochemical water splitting. *Chem. Soc. Rev.* **43**, 7520–7535 (2014).
6. Maeda, K. & Domen, K. Photocatalytic water splitting: recent progress and future challenges. *J. Phys. Chem. Lett.* **1**, 2655–2661 (2010).
7. Li, R. et al. Spatial separation of photogenerated electrons and holes among {010} and {110} crystal facets of BiVO_4 . *Nat. Commun.* **4**, 1432 (2013).
8. Takata, T. et al. Photocatalytic water splitting with a quantum efficiency of almost unity. *Nature* **581**, 411–414 (2020).
9. Bavykina, A. et al. Metal–organic frameworks in heterogeneous catalysis: recent progress, new trends, and future perspectives. *Chem. Rev.* **120**, 8468–8535 (2020).

10. Gan, X., Lei, D. & Wong, K.-Y. Two-dimensional layered nanomaterials for visible-light-driven photocatalytic water splitting. *Mater. Today Energy* **10**, 352–367 (2018).
11. Wang, Q. & Domen, K. Particulate photocatalysts for light-driven water splitting: mechanisms, challenges, and design strategies. *Chem. Rev.* **120**, 919–985 (2020).
12. Yuan, S. et al. Covalent organic frameworks for membrane separation. *Chem. Soc. Rev.* **48**, 2665–2681 (2019).
13. Ying, Y. et al. Ultrathin two-dimensional membranes assembled by ionic covalent organic nanosheets with reduced apertures for gas separation. *J. Am. Chem. Soc.* **142**, 4472–4480 (2020).
14. Fan, H. et al. MOF-in-COF molecular sieving membrane for selective hydrogen separation. *Nat. Commun.* **12**, 38 (2021).
15. Li, J. et al. Bulk COFs and COF nanosheets for electrochemical energy storage and conversion. *Chem. Soc. Rev.* **49**, 3565–3604 (2020).
16. Li, M. et al. Skeleton engineering of isostructural 2D covalent organic frameworks: orthoquinone redox-active sites enhanced energy storage. *CCS Chem.* **2**, 696–706 (2020).
17. Li, C. et al. Pristine MOF and COF materials for advanced batteries. *Energy Storage Mater.* **31**, 115–134 (2020).
18. Shi, R. et al. Nitrogen-rich covalent organic frameworks with multiple carbonyls for high-performance sodium batteries. *Nat. Commun.* **11**, 178 (2020).
19. Liu, X. et al. Recent advances in covalent organic frameworks (COFs) as a smart sensing material. *Chem. Soc. Rev.* **48**, 5266–5302 (2019).
20. Li, Z. et al. Editing light emission with stable crystalline covalent organic frameworks via wall surface perturbation. *Angew. Chem. Int. Ed.* **60**, 19419–19427 (2021).
21. Li, Y.-J. et al. A general design approach toward covalent organic frameworks for highly efficient electrochemiluminescence. *Nat. Commun.* **12**, 4735 (2021).
22. Evans, A. M. et al. High-sensitivity acoustic molecular sensors based on large-area, spray-coated 2D covalent organic frameworks. *Adv. Mater.* **32**, 2004205 (2020).
23. Liu, J., Wang, N. & Ma, L. Recent advances in covalent organic frameworks for catalysis. *Chem. Asian J.* **15**, 338–351 (2020).
24. Ma, H.-C., Zou, J., Li, X.-T., Chen, G.-J. & Dong, Y.-B. Homochiral covalent organic frameworks for asymmetric catalysis. *Chem. Eur. J.* **26**, 13754–13770 (2020).
25. Guo, J. & Jiang, D. Covalent organic frameworks for heterogeneous catalysis: principle, current status, and challenges. *ACS Cent. Sci.* **6**, 869–879 (2020).
26. Zhi, Y., Wang, Z., Zhang, H.-L. & Zhang, Q. Recent progress in metal-free covalent organic frameworks as heterogeneous catalysts. *Small* **16**, 2001070 (2020).
27. Li, C. et al. Asymmetric photocatalysis over robust covalent organic frameworks with tetrahydroquinoline linkage. *Chin. J. Catal.* **41**, 1288–1297 (2020).

28. Liu, Y. et al. Spirobifluorene-based three-dimensional covalent organic frameworks with rigid topological channels as efficient heterogeneous catalyst. *CCS Chem.* **2**, 2418–2427 (2020).
29. Cao, Q. et al. Covalent organic framework-supported Zn single atom catalyst for highly efficient N-formylation of amines with CO₂ under mild conditions. *Appl. Catal. B* **294**, 120238 (2021).
30. Sun, Q. et al. Reaction environment modification in covalent organic frameworks for catalytic performance enhancement. *Angew. Chem. Int. Ed.* **58**, 8670–8675 (2019).
31. Rahman, M., Tian, H. & Edvinsson, T. Revisiting the limiting factors for overall water-splitting on organic photocatalysts. *Angew. Chem. Int. Ed.* **59**, 16278–16293 (2020).
32. Xu, J. et al. Vinylene-linked covalent organic frameworks (COFs) with symmetry-tuned polarity and photocatalytic activity. *Angew. Chem. Int. Ed.* **59**, 23845–23853 (2020).
33. Guo, L., Niu, Y., Razzaque, S., Tan, B. & Jin, S. Design of D–A₁–A₂ covalent triazine frameworks via copolymerization for photocatalytic hydrogen evolution. *ACS Catal.* **9**, 9438–9445 (2019).
34. Zhao, Z. et al. Fabrication of robust covalent organic frameworks for enhanced visible-light-driven H₂ evolution. *ACS Catal.* **11**, 2098–2107 (2021).
35. Zhang, S. et al. Strong-base-assisted synthesis of a crystalline covalent triazine framework with high hydrophilicity via benzylamine monomer for photocatalytic water splitting. *Angew. Chem. Int. Ed.* **59**, 6007–6014 (2020).
36. Chen, W. et al. Modulating benzothiadiazole-based covalent organic frameworks via halogenation for enhanced photocatalytic water splitting. *Angew. Chem. Int. Ed.* **59**, 16902–16909 (2020).
37. Wang, X. et al. Sulfone-containing covalent organic frameworks for photocatalytic hydrogen evolution from water. *Nat. Chem.* **10**, 1180–1189 (2018).
38. Wei, S. et al. Semiconducting 2D triazine-cored covalent organic frameworks with unsubstituted olefin linkages. *J. Am. Chem. Soc.* **141**, 14272–14279 (2019).
39. Jin, E. et al. 2D sp² carbon-conjugated covalent organic frameworks for photocatalytic hydrogen production from water. *Chem* **5**, 1632–1647 (2019).
40. Mo, C. et al. Alkene-linked covalent organic frameworks boosting photocatalytic hydrogen evolution by efficient charge separation and transfer in the presence of sacrificial electron donors. *Adv. Sci.* **7**, 1902988 (2020).
41. Lin, L. et al. Molecular-level insights on the reactive facet of carbon nitride single crystals photocatalysing overall water splitting. *Nat. Catal.* **3**, 649–655 (2020).
42. Yang, et al. Side-chain isomerization on an n-type organic semiconductor ITIC acceptor makes 11.77% high efficiency polymer solar cells. *J. Am. Chem. Soc.* **138**, 15011–15018 (2016).
43. Zhu, W. et al. Crystallography, morphology, electronic structure, and transport in non-fullerene/non-indacenodithienothiophene polymer:Y6 solar cells. *J. Am. Chem. Soc.* **142**, 14532–14547 (2020).

44. Yuan, J. et al. Single-junction organic solar cell with over 15% efficiency using fused-ring acceptor with electron-deficient core. *Joule* **3**, 1140–1151 (2019).
45. Wang, K. et al. Covalent triazine frameworks via a low-temperature polycondensation approach. *Angew. Chem. Int. Ed.* **56**, 14149–14153 (2017).
46. Chandra, S. et al. Chemically stable multilayered covalent organic nanosheets from covalent organic frameworks via mechanical delamination. *J. Am. Chem. Soc.* **135**, 17853–17861 (2013).
47. Li, C. et al. One-pot synthesis of mesosilica/nano covalent organic polymer composites and their synergistic effect in photocatalysis. *Chin. J. Catal.* **42**, 1821–1830 (2021).
48. Xu, H., Gao, J. & Jiang, D. Stable, crystalline, porous, covalent organic frameworks as a platform for chiral organocatalysts. *Nat. Chem.* **7**, 905–912 (2015).
49. Khayum, M. A. et al. Chemically delaminated free-standing ultrathin covalent organic nanosheets. *Angew. Chem. Int. Ed.* **55**, 15604–15608 (2016).
50. Umezawa, K., Nakamura, Y., Makino, H., Citterio, D. & Suzuki, K. Bright, color-tunable fluorescent dyes in the visible-near-infrared region. *J. Am. Chem. Soc.* **130**, 1550–1551 (2008).
51. Zhang, P., Wang, T., Chang, X. & Gong, J. Effective charge carrier utilization in photocatalytic conversions. *Acc. Chem. Res.* **49**, 911–921 (2016).
52. Ren, X. et al. Enormous promotion of photocatalytic activity through the use of near-single layer covalent organic frameworks. *CCS Chem.* **3**, 2453–2463 (2021).
53. Wang, Z. et al. Efficiency accreditation and testing protocols for particulate photocatalysts toward solar fuel production. *Joule* **5**, 344–359 (2021).
54. Liu, M. et al. Crystalline covalent triazine frameworks by in situ oxidation of alcohols to aldehyde monomers. *Angew. Chem. Int. Ed.* **57**, 11968–11972 (2018).
55. Bi, S. et al. Two-dimensional semiconducting covalent organic frameworks via condensation at arylmethyl carbon atoms. *Nat. Commun.* **10**, 2467 (2019).
56. Chen, R. et al. Rational design of isostructural 2D porphyrin-based covalent organic frameworks for tunable photocatalytic hydrogen evolution. *Nat. Commun.* **12**, 1354 (2021).
57. Mi, Z. et al. Covalent organic frameworks enabling site isolation of viologen-derived electron-transfer mediators for stable photocatalytic hydrogen evolution. *Angew. Chem. Int. Ed.* **60**, 9642–9649 (2021).
58. Wang, D. et al. Highly efficient charge transfer in CdS-covalent organic framework nanocomposites for stable photocatalytic hydrogen evolution under visible light. *Sci. Bull.* **65**, 113–122 (2020).
59. Li, C.-C. et al. Rational combination of covalent-organic framework and nano TiO₂ by covalent bonds to realize dramatically enhanced photocatalytic activity. *Appl. Catal. B* **266**, 118586 (2020).
60. Luo, M., Yang, Q., Liu, K., Cao, H. & Yan, H. Boosting photocatalytic H₂ evolution on g-C₃N₄ by modifying covalent organic frameworks (COFs). *Chem. Commun.* **55**, 5829–5832 (2019).

61. Luo, M. et al. Defects engineering leads to enhanced photocatalytic H₂ evolution on graphitic carbon nitride-covalent organic framework nanosheet composite. *Small* **16**, 2001100 (2020).
62. Zhou, T. et al. PEG-stabilized coaxial stacking of two-dimensional covalent organic frameworks for enhanced photocatalytic hydrogen evolution. *Nat. Commun.* **12**, 3934 (2021).
63. Xing, Y. Construction of the 1D covalent organic framework/2D g-C₃N₄ heterojunction with high apparent quantum efficiency at 500 nm. *ACS Appl. Mater. Interfaces* **12**, 51555–51562 (2020).
64. Shu, C. et al. Boosting the photocatalytic hydrogen evolution activity for D-π-A conjugated microporous polymers by statistical copolymerization. *Adv. Mater.* **33**, 2008498 (2021).
65. Zhang, X., Peng, B., Zhang, S. & Peng, T. Robust wide visible-light-responsive photoactivity for H₂ production over a polymer/polymer heterojunction photocatalyst: the significance of sacrificial reagent. *ACS Sustainable Chem. Eng.* **3**, 1501–1509 (2015).
66. She, X. et al. High efficiency photocatalytic water splitting using 2D α-Fe₂O₃/g-C₃N₄ Z-Scheme Catalysts. *Adv. Energy Mater.* **7**, 1700025 (2017).
67. Zhang, J. et al. High quantum yield blue emission from lead-free inorganic antimony halide perovskite colloidal quantum dots. *ACS Nano* **11**, 9294–9302 (2017).
68. Sun, S. et al. The origin of high efficiency in low-temperature solution-processable bilayer organometal halide hybrid solar cells. *Energy Environ. Sci.* **7**, 399–407 (2014).

Declarations

Acknowledgment

This work was supported by the National Key R&D Program of China (2017YFB0702800), the National Natural Science Foundation of China (21733009, 22002162) and the Strategic Priority Research Program of the Chinese Academy of Sciences (XDB17020200). J.W. thanks the financial support from the National Natural Science Foundation of China (21973091) and the Youth Innovation Promotion Association CAS (2021185). We acknowledge Dr. Ting Yang for assistance with the PL measurement. C.L. thanks Dr. Fangfang Xu and Ms. Xiaomin Ren for helpful discussions.

Author contributions

C.L. did most of the experiments, structure simulation and wrote the manuscript; J.L. helped with SEM characterization; K.W. helped with TA characterization and analysis; Q.Y., H.L. and J.W. designed and supervised the project. The manuscript was written through contributions of all authors.

Supplementary Information

Supplementary Information accompanies this paper at <http://xxx>.

Competing interest

The authors declare no competing interests.

Figures

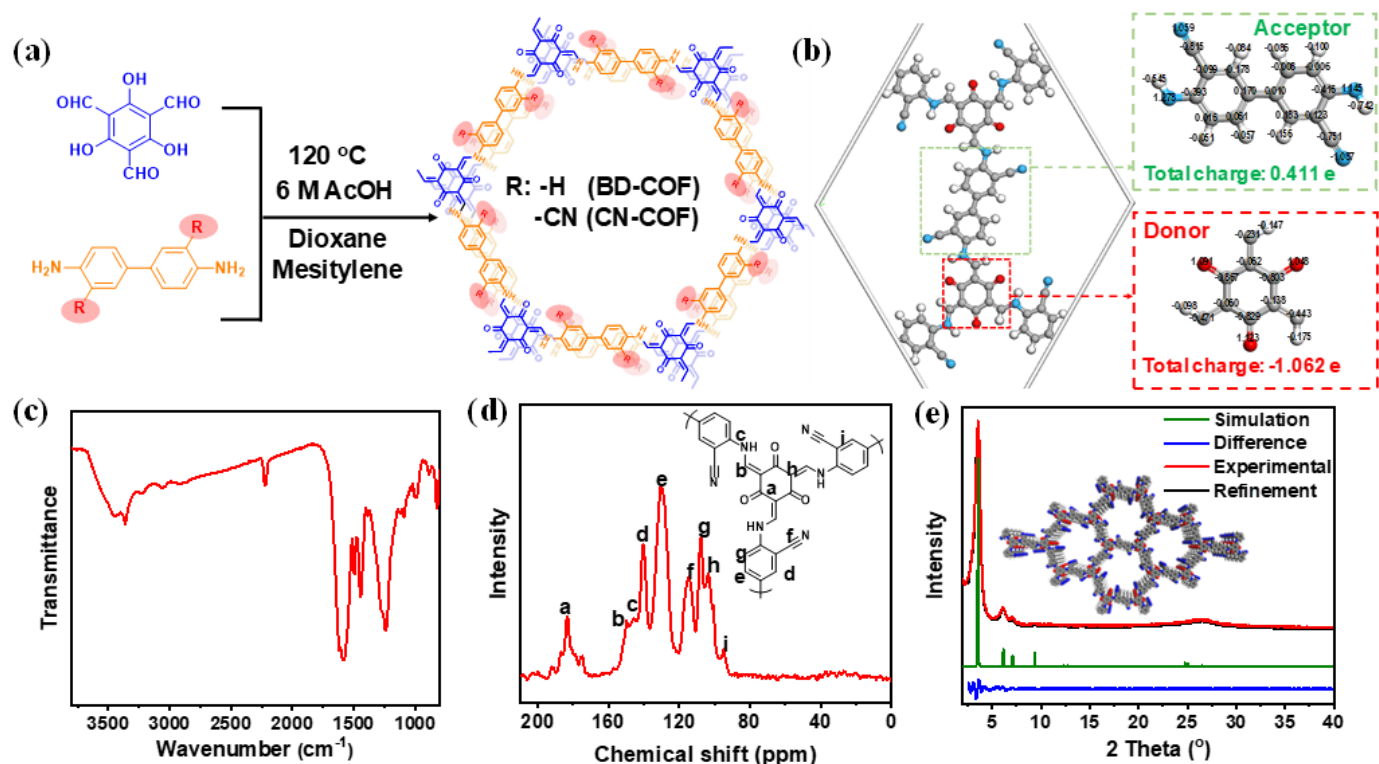


Figure 1

Chemical structure, charge distribution, and characterizations of CN-COF. (a) Synthesis of CN-COF and BD-COF. (b) Charge distribution in CN-COF structure. (c) FT-IR spectrum of CN-COF. (d) Solid state ¹³C CP-TOSS NMR spectrum of CN-COF. (e) Experimental (red), simulated (green), refined (black) PXRD patterns and the refinement differences (blue) of CN-COF.

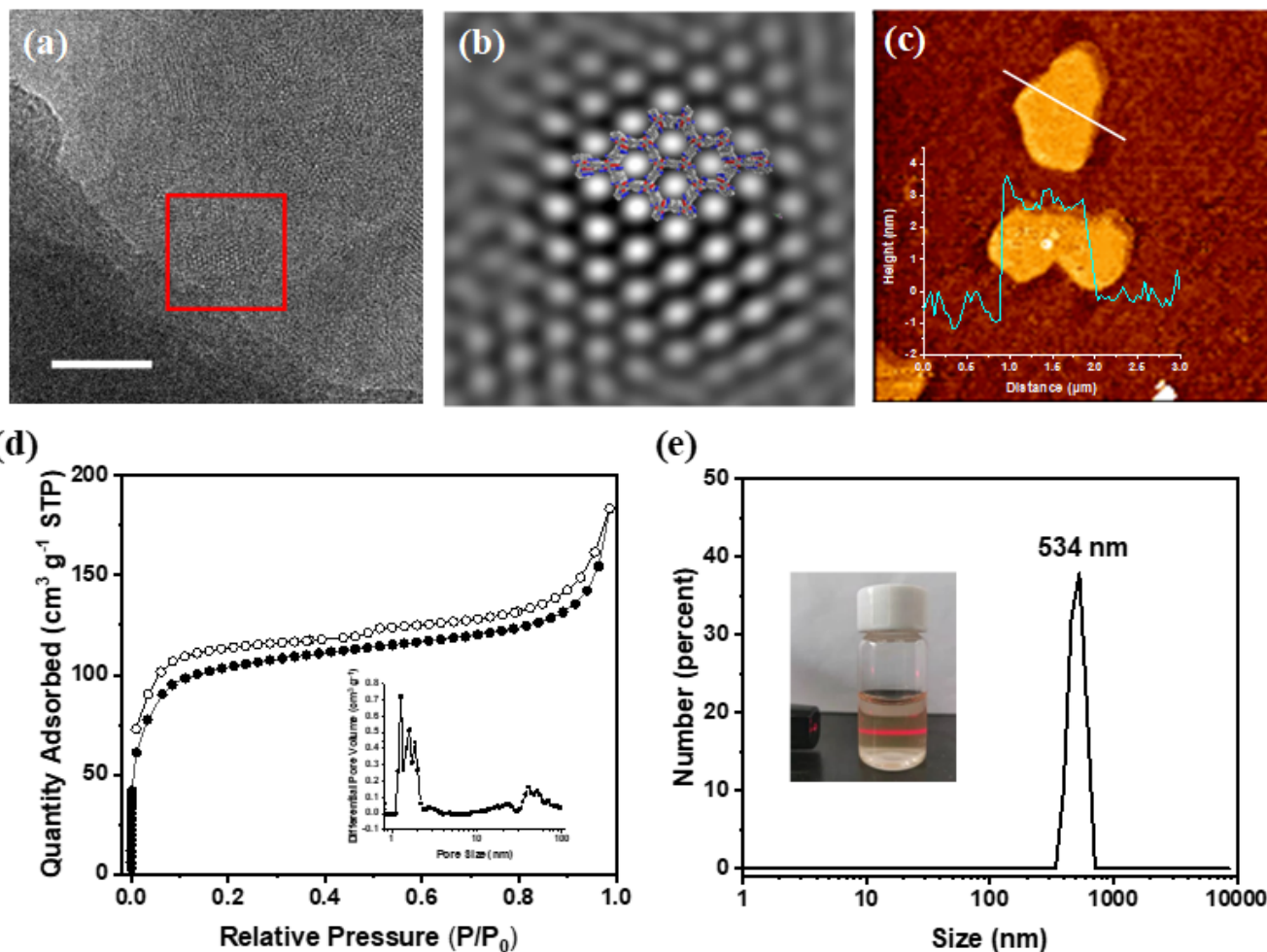


Figure 2

Characterizations of CN-CON (obtained by ball milling of CN-COF). (a) HR-TEM image (scale bar, 50 nm), and (b) Fourier-filtered image of selected red square area (scale bar, 5 nm). (c) AFM image (Inset: height plot). (d) Nitrogen sorption isotherms at 77 K and pore size distribution (inset). (e) Particle size distribution by dynamic light scattering (Inset: photograph of colloidal solution after 4 months and observed Tyndall effect).

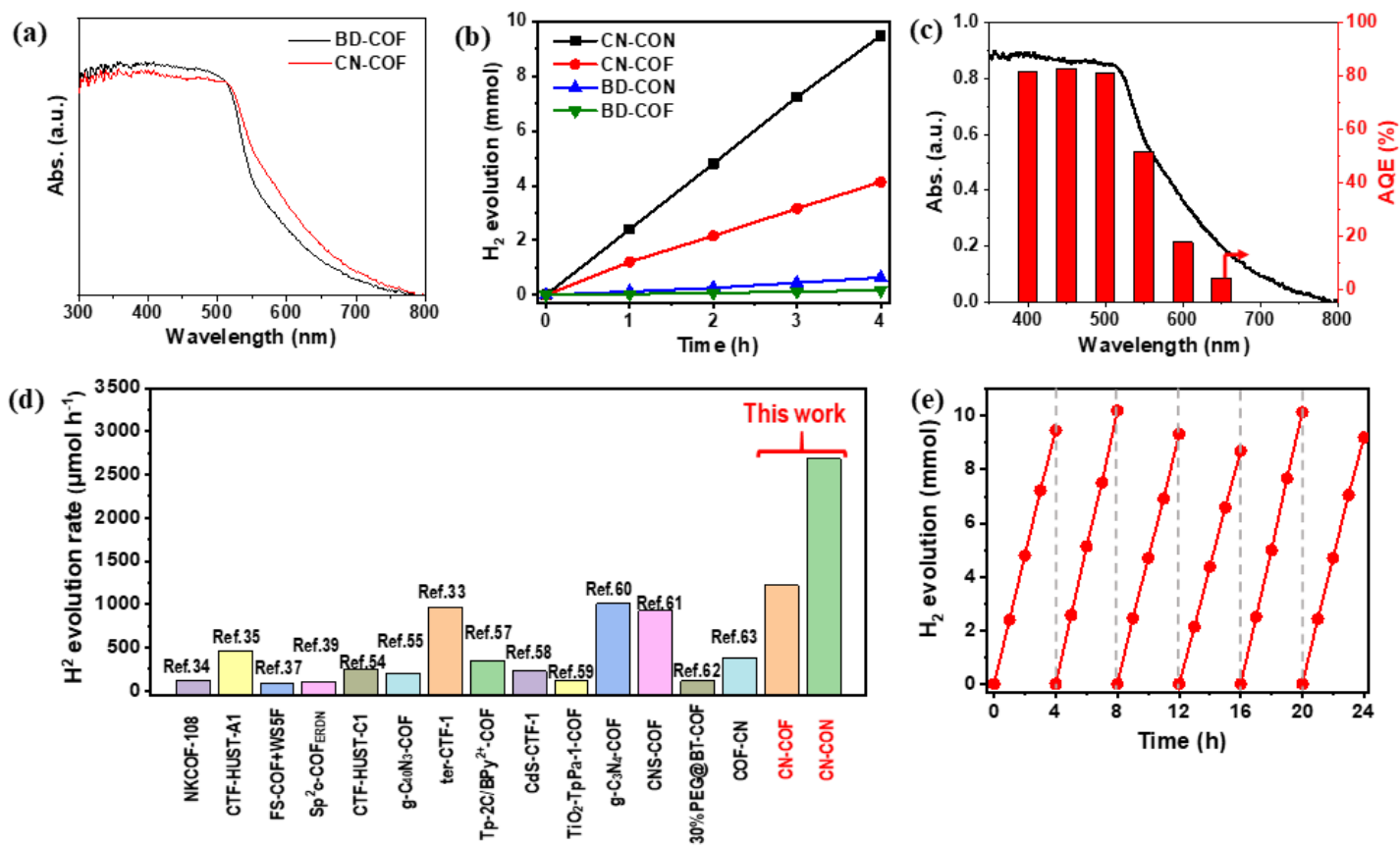


Figure 3

Absorption spectra, and photocatalytic H₂ evolution. (a) UV-vis DRS spectra of BD-COF and CN-COF. (b) Time course of photocatalytic H₂ production for different COFs and CONs (20 mg catalyst in 100 mL water, 1 wt% Pt, 10 mmol ascorbic acid, $\lambda > 420$ nm). (c) Wavelength-dependent AQE of photocatalytic H₂ production for CN-CON. (d) Photocatalytic H₂ production activities for previous representative COFs and COFs composite materials. (e) Cycling stability for CN-CON in photocatalytic H₂ production.

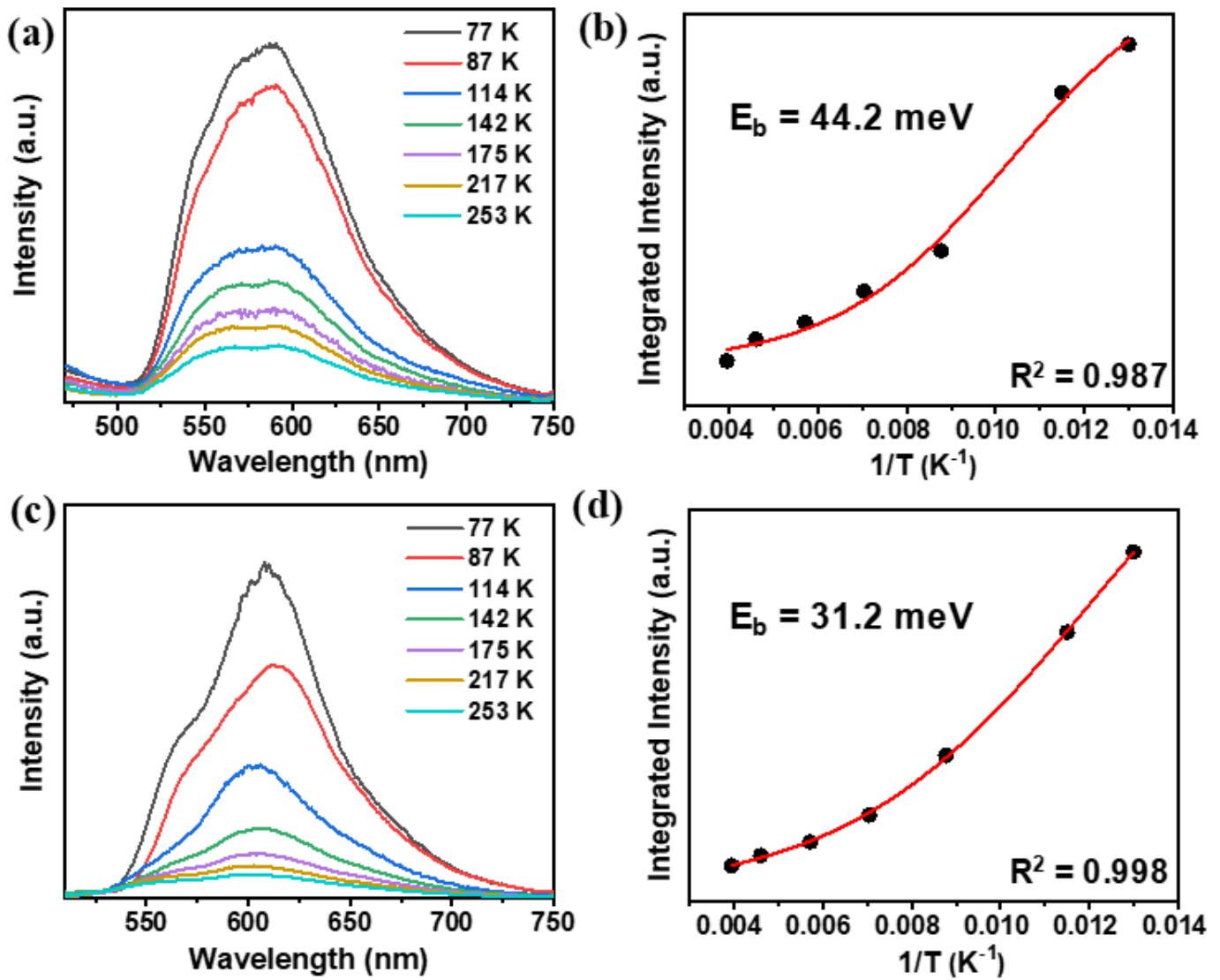


Figure 4

Exciton binding energies measurement. Temperature-dependent PL spectra with excitation wavelength at 380 nm and extracted exciton binding energies of (a-b) BD-CON and (c-d) CN-CON.

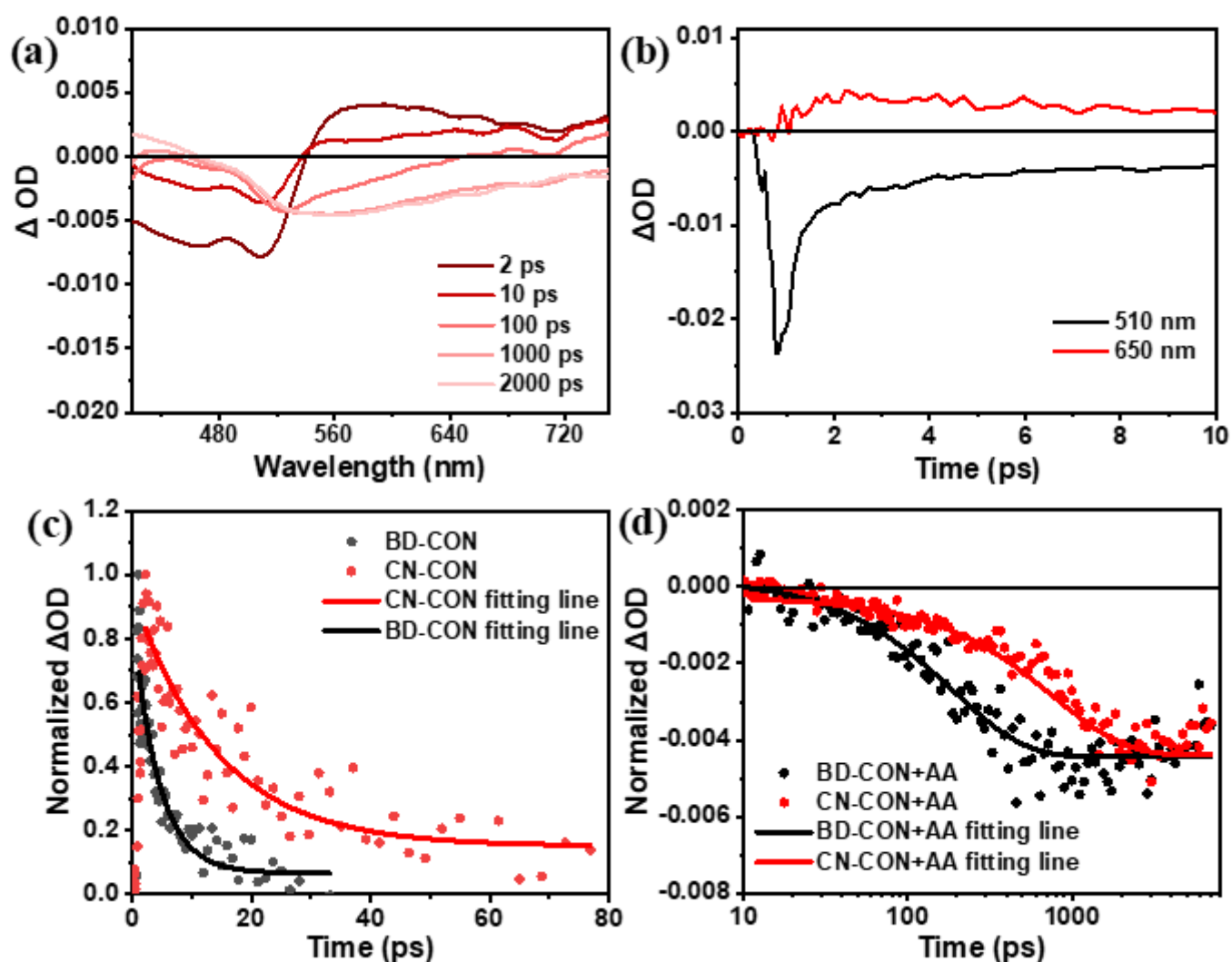


Figure 5

Femtosecond transient absorption measurements. TA details of CN-CON and BD-CON pumped at 400 nm. (a) Time slices of the TA spectra of CN-CON in water. (b) TA kinetics of CN-CON probed at 510 nm (GSB) and 650 nm (trapped hole). Comparison of the kinetics for CN-CON and BD-CON (c) probed at 650 nm (0-80 ps for trapped hole) and (d) probed at 650 nm (10-8000 ps for long-lived free electron) in the presence of 0.1 M ascorbic acid.

Supplementary Files

This is a list of supplementary files associated with this preprint. Click to download.

- [Sl.pdf](#)
- [Slvideo.mp4](#)